

Article

Exciton–Phonon Interactions in Strained Domes of Monolayer MoS₂ Studied by Resonance Raman Spectroscopy

Jessica S. Lemos^{1,*} , Elena Blundo² , Antonio Polimeni² , Marcos A. Pimenta^{1,3}  and Ariete Righi^{1,*} 

¹ Departamento de Física, Universidade Federal de Minas Gerais, Belo Horizonte 31270-901, MG, Brazil; mpimenta@fisica.ufmg.br

² Dipartimento di Fisica, Sapienza Università di Roma, 00185 Roma, Italy; elena.blundo@uniroma1.it (E.B.); antonio.polimeni@uniroma1.it (A.P.)

³ Departamento de Física, Universidade Federal do Ouro Preto, Campus Universitário Morro do Cruzeiro, ICEB, Ouro Preto 35400-000, MG, Brazil

* Correspondence: jsantoslemos@ufmg.br (J.S.L.); righi@fisica.ufmg.br (A.R.)

Abstract: This work describes a resonance Raman study performed in the domes of monolayer MoS₂ using 23 different laser excitation energies covering the visible and near-infrared (NIR) ranges. The multiple excitation results allowed us to investigate the exciton–phonon interactions of different phonons (A₁['], E', and LA) with different excitonic optical transitions in biaxially strained monolayer MoS₂. The analysis of the intensities of the two first-order peaks, A₁['] and E', and the double-resonance 2LA Raman band as a function of the laser excitation furnished the values of the energies of the indirect exciton and the direct excitonic transitions in the strained MoS₂ domes. It was noticed that the out-of-plane A₁['] phonon mode is significantly enhanced only by the indirect exciton I and the C exciton, whereas the in-plane E' mode is only enhanced by the C exciton of the MoS₂ dome, thus revealing the weak interaction of these phonons with the A and B excitons in the strained MoS₂ domes. On the other hand, the 2LA Raman band is significantly enhanced at the indirect exciton I and by the A (or B) exciton but not enhanced by the C exciton, thus showing that the LA edge phonons that participate in the double-resonance process in MoS₂ have a weak interaction with the C exciton.

Keywords: MoS₂ dome; Raman excitation profile; biaxial strain



Citation: Lemos, J.S.; Blundo, E.; Polimeni, A.; Pimenta, M.A.; Righi, A. Exciton–Phonon Interactions in Strained Domes of Monolayer MoS₂ Studied by Resonance Raman Spectroscopy. *Nanomaterials* **2023**, *13*, 2722. <https://doi.org/10.3390/nano13192722>

Academic Editor: Maciej Molas

Received: 18 August 2023

Revised: 26 September 2023

Accepted: 1 October 2023

Published: 7 October 2023



Copyright: © 2023 by the authors. Licensee MDPI, Basel, Switzerland. This article is an open access article distributed under the terms and conditions of the Creative Commons Attribution (CC BY) license (<https://creativecommons.org/licenses/by/4.0/>).

1. Introduction

Two-dimensional (2D) materials exhibit unique properties that depend on various factors, including the material's chemical composition, atomic arrangement, thickness, and interlayer interactions [1,2]. Modification of the intrinsic properties of crystalline materials is often necessary to achieve new fundamental effects or create favorable conditions for device fabrication. By carefully tuning these parameters, researchers can unlock new properties and behaviors in solid-state materials, leading to innovative technologies and scientific discoveries [2–4]. Recent studies have explored the effects of mechanical deformation and stress on the properties of 2D materials [5–9]. In particular, the ability of 2D materials to be easily strained is of great interest, as strain engineering can significantly impact their electronic and optical properties [8,10–16]. Indeed, many theoretical works have predicted that biaxial strain is particularly effective in tuning the band structure of transition metal dichalcogenides (TMDs) [17–22].

Atomically thin materials of the MoS₂-type family are particularly well-suited for studying the effects of mechanical deformation and stress, because they can withstand extreme nonhomogeneous deformations before rupture [9,23–29]. The electronic and optical properties of MoS₂ monolayers are strongly coupled to the valley/spin/orbital degrees of freedom and the lattice structure, making them sensitive to mechanical deformation or stress [5,11,25,30–32]. To explore the effect of biaxial strain on TMDs, various methods have been developed, such as deposition on nanocones [33] or pillars [34] and the epitaxial

growth of superlattices [35]. In these methods, the strain obtained is typically around 1–2%. However, values of strain of 5% are reached at the center of the MoS₂ monolayer domes that are investigated in this work [11,36].

In this paper, we present a resonant Raman spectroscopy study of an MoS₂ dome sample using 23 different laser excitation energies in the NIR and visible ranges. Our measurements allowed us to obtain the Raman excitation profiles (REPs) of the first-order E' and A'₁ Raman modes, as well as the REP of the second-order 2LA Raman band. Our results show that the three Raman bands are significantly enhanced at the indirect exciton transition at 1.61 eV and by the C exciton at 2.72 eV, but the interaction of the first-order modes with the A and B excitons was shown to be very weak in the strained MoS₂ dome. Redshifts were also observed in the energies of the A and B excitons, in agreement with previous photoluminescence (PL) results [11,18,21,37], as well as in the energy of the C exciton. In fact, the multiple excitation Raman study in strained MoS₂ presented in this work is the first report of the REPs of the first- and second-order bands in strained MoS₂ and, as far as we know, the redshift that we observed for the C exciton in MoS₂ domes has not yet been reported in the literature. Our work provides important insights into the effects of biaxial strain on the excitonic and optical properties of 2D materials, which could have implications for the development of innovative technologies and scientific discoveries.

2. Materials and Methods

Figure 1a displays an optical image of an MoS₂ dome, created according to the procedure outlined by Tedeschi et al. [38] to generate isolates or conglomerates of semispherical nano- and micrometric domes. Raman maps were acquired using a Horiba LabRAM HR Evolution spectrometer equipped with a grating of 1800 lines/mm. A NIKON objective with a magnification of 100× and numerical aperture of 0.9 was used, and the laser energy of 2.34 eV was set to a power of 100 μW to prevent heating and bursting of the dome. In addition to this configuration, another piece of equipment was utilized, the HORIBA T64000 triple monochromator spectrometer, using different laser sources and 23 laser excitation energies, covering a wide range of energies from 1.59 to 2.73 eV. Specifically, the Ar-Kr laser was used for excitation energies from 2.73 to 1.92 eV, and the Ti-Sapphire laser, pumped by a VERDI laser at 532 nm, covered the excitation energy range from 1.69 to 1.59 eV. Two solid-state lasers at 1.88 eV and 2.09 eV and one He-Ne laser at 1.96 eV were also used. An objective of 100× magnification and a laser power of around 10 μW were used to avoid heating and bursting of the dome. Raman measurements were performed with linearly polarized lasers but without an analyzer for the scattered light. All measurements were realized at room temperature with a backscattering configuration.

The photoluminescence measurements were conducted using a HORIBA T64000 triple-monochromator spectrometer in a single mode, which was equipped with a grating of 300 lines/mm. The excitation was carried out with a VERDI laser that has an energy of 2.33 eV. A 100× magnification objective was employed, with the laser power set to approximately 100 μW. These measurements were performed at room temperature, employing a backscattering configuration.

3. Results

We began our study by characterizing the Raman modes of a selected dome. Figure 1 presents the optical image, Raman spectra, and intensity Raman maps acquired, as well as the positions of the A'₁ and E' modes from the sample. The dashed circles around the dome delineate its edge. Figure 1a shows that the semispherical dome has a diameter of approximately $(2.4 \pm 0.1) \mu\text{m}$. Figure 1b presents the Raman spectra recorded at the center of the dome (black line) and at the MoS₂ bulk substrate (red line) with 2.34 eV laser energy. The bulk's Raman spectrum exhibits two modes, E_{2g} and A_{1g}, located around 384 cm⁻¹ and 409 cm⁻¹, respectively [39,40]. The Raman spectra at the dome's center exhibit four modes, where the two weaker peaks come from the bulk's substrate and the two more intense peaks, shifted to lower wavenumbers around 373 cm⁻¹ and 402 cm⁻¹, are

associated with the E' and A'_1 modes of the monolayer dome, respectively. In the literature, the positions of the E' and A'_1 modes in unstrained monolayer MoS_2 are 385 cm^{-1} and 404 cm^{-1} , respectively [40–42]. Therefore, the redshifts in the mode positions of the strained monolayer MoS_2 studied in this work with respect to the unstrained monolayer MoS_2 are 12 cm^{-1} and 2 cm^{-1} for the E' and A'_1 modes, respectively [42]. Previous studies have shown that the effect of the biaxial strain at the dome is more significant for the E' mode, with a displacement rate of $2.2\text{ cm}^{-1}/\%$ [5]. According to this relation, the shift of 12 cm^{-1} observed in our work for the E' mode corresponds to a value of $\approx 5.5\%$ of strain at the dome's center, shown in Figure 1a.

Figure 1c–f shows the intensity maps and positions of the dome peaks acquired with a laser energy of 2.34 eV. The intensity maps of the E' and A'_1 Raman peaks indicate an increase in the modes intensities at the dome's region compared with the bulk spectra, as displayed in Figure 1c,d, respectively. The positions of the E' and A'_1 Raman peaks at the monolayer dome's center are redshifted by about 11 cm^{-1} and 7 cm^{-1} , respectively, when compared with the bulk's positions, as shown in Figures 1e,f, respectively.

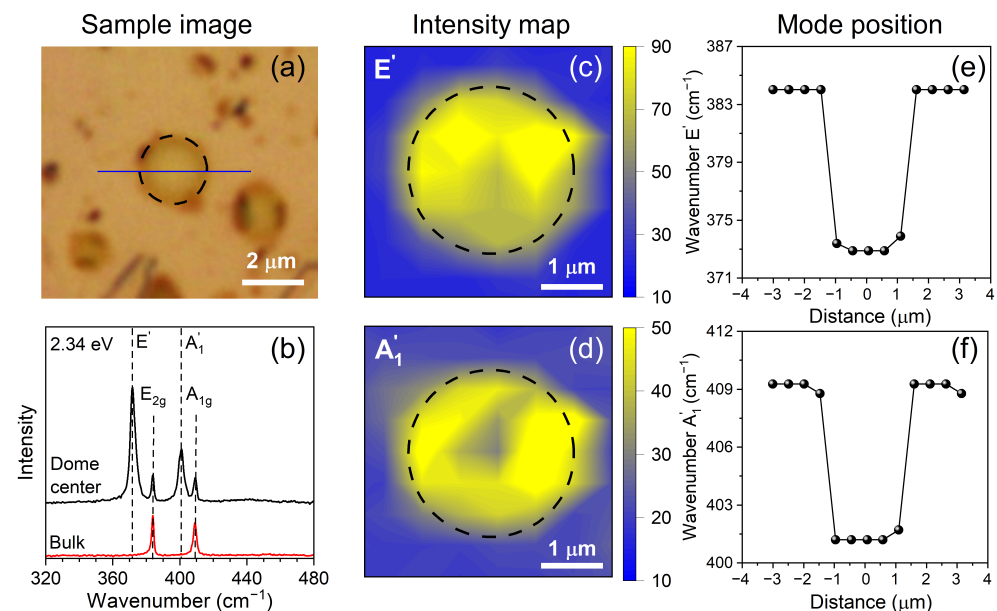


Figure 1. (a) Optical image of the sample. The dome edge is delimited by a black dashed line. (b) Raman spectra of the dome center (black) and of the MoS_2 bulk flake (red) acquired with excitation energy of 2.34 eV. (c,d) Intensity Raman maps of the first-order Raman modes E' and A'_1 , respectively. (e,f) Positions of first-order Raman modes, E' and A'_1 , measured along the blue line shown in Figure 1a, respectively.

Figure 2a shows the Raman spectra recorded at the dome's center using five different laser excitation energies: 1.59 eV (780 nm), 1.68 eV (738 nm), 1.92 eV (646 nm), 2.38 eV (521 nm), and 2.73 eV (454 nm). The three dashed lines serve as guides to follow the positions of the in-plane E' , the out-of-plane A'_1 , and the 2LA modes. The Raman spectra of the bulk sample were subtracted from the spectra so that it only displays the peaks of the dome's center. In addition to the first-order modes, we can observe the second-order 2LA Raman band [43] centered around 440 cm^{-1} .

In the spectrum of the 1.59 eV excitation energy, we can observe an intense and sharp peak associated with the out-of-plane A'_1 mode and the broad 2LA band. Notice that the in-plane E' mode is absent in this spectrum. In the 1.68 eV excitation energy spectrum, the A'_1 mode is still the most intense, the 2LA band is observed, and we can see the appearance of a broad band in the position of the E' mode. In the 1.92 eV excitation energy spectrum, we can observe that the broad 2LA band becomes the most intense, and the appearance of the E' mode is clearly observed. The broad band near the position of the E' mode is related to a double-resonance Raman process involving different valleys of MoS_2 [43]. By increasing

the excitation energy, we can observe in the 2.38 eV excitation energy spectrum that the E' mode becomes as intense as the A'_1 mode, and the 2LA band is absent in the spectrum. In the highest 2.73 eV excitation energy spectrum, we see that the E' mode becomes more intense than the A'_1 mode.

Figure 2b shows the result of a multiple excitation energy Raman map at the MoS₂ dome's center obtained using 23 different laser lines with excitation energies ranging from 1.59 to 2.73 eV. The peak intensities in Figure 2b were normalized by the intensity of the 465 cm⁻¹ Raman mode of quartz and are represented by the color bar. The intensity of the Raman spectrum of quartz has no dependence on the laser excitation energy since its band gap is in the UV range, around 8 eV [44,45] and, therefore, there is no resonance Raman effect in quartz in the visible range. The energies of the incident photons are on the vertical scale, and the horizontal scale represents the Raman shifts. The blank gap in excitation energies between 1.69 and 1.88 eV in Figure 2b is a region where we do not have available laser lines.

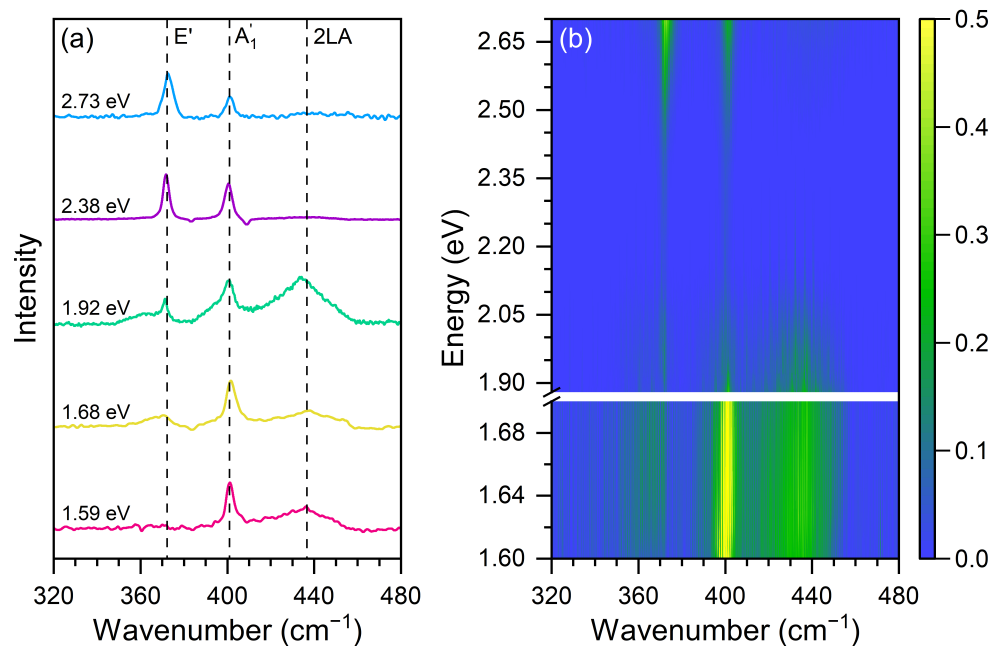


Figure 2. (a) Raman spectra of the MoS₂ dome center with five excitation energies: 1.59 eV (pink line), 1.68 eV (yellow line), 1.92 eV (green line), 2.38 eV (purple line), and 2.73 eV (blue line). (b) Raman map of the dome center with twenty-three laser lines with photon energies in the Vis–NIR range.

Figure 3 shows the Raman excitation profiles (REPs) of the A'_1 , E' , and 2LA bands, that is, the intensity of each feature as a function of the laser excitation energy. We discuss the results of the first-order modes and the 2LA band separately. The REPs of the first-order A'_1 (open red squares) and E' (dark blue triangles) modes are shown in Figure 3, and the lines represent the best fits of the experimental data considering the equation for Raman intensity as a function of the laser energy E_L for a first-order (one-phonon) process given by [46]

$$I^k(E_L) = \sum_i \left| \frac{M_{\text{el-rad}} \cdot M_{\text{ex-ph}}^{(i)-(k)} \cdot M_{\text{el-rad}}}{(E_L - E_{\text{ex}}^i - i\gamma^i)(E_L - E_{\text{ph}}^k - E_{\text{ex}}^i - i\gamma^i)} \right|^2, \quad (1)$$

where the index i denotes the excitonic transition, the index k denotes the two phonons (A'_1 or E'), and the three terms in the numerator represent the matrix elements of the electron–radiation (absorption of the incident photon), exciton–phonon, and electron–radiation (emission of the scattered photon) interactions, respectively. The two terms in the denominator give rise to the resonant enhancement of the Raman peaks when the incident or

scattered photon energies match the exciton energy. The damping constant γ^i is related to the finite lifetime of the exciton i involved in the Raman process, where E_{ex}^i is the energy of exciton i , and E_{ph}^k is the energy of phonon k .

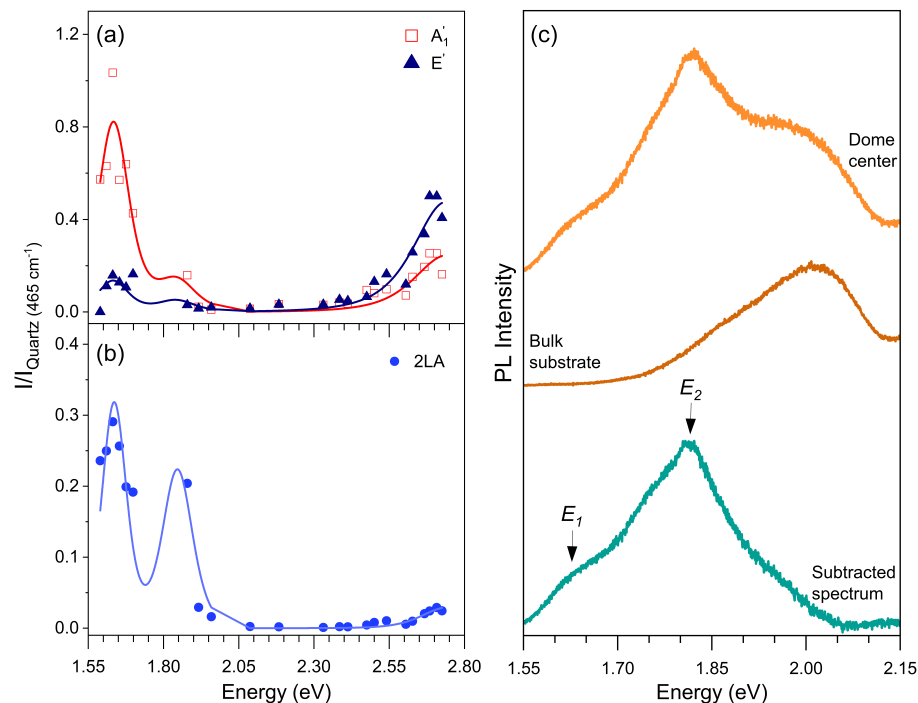


Figure 3. (a) Raman excitation profile (REP) of the first-order Raman modes E' (dark blue triangles) and A'_1 (open red squares). (b) REP of the 2LA Raman band (blue circles). (c) Photoluminescence spectrum acquired at the dome center (orange), MoS₂ bulk substrate (brown), and subtracted spectrum (green) resulting from the difference between the dome center and bulk spectra. The arrows indicate the values of the resonance energies obtained in the REP.

Figure 3a clearly shows three resonances in the REPs in the investigated range of energies. Notice that the out-of-plane A'_1 mode is enhanced by the three resonances, whereas the in-plane E' mode is weakly enhanced at lower energies but is more intense than the A'_1 mode at higher energies in Figure 3a.

In the fitting process, the same set of parameters of the excitons (energies and damping constants) was used to fit the REPs of the different phonon modes. Table 1 shows the fitting parameters (exciton energies and damping constants) that provide the best fit of the experimental REP data and are represented by the solid curves in Figure 3a. The values for the first resonance (E_1) are more accurate, since we have more experimental data in this energy region. The lack of experimental points in the range 1.69–1.88 eV prevented us from measuring with accuracy the second resonance (E_2) energy and linewidth. The accuracy in the value of the third resonance energy (E_3) is also poor, since we do not have experimental points above 2.8 eV.

Table 1. Energies and damping constants of the observed resonances in the Raman excitation profile in strained MoS₂.

Resonance	Energy (eV)	Damping (eV)
E_1	1.61 ± 0.01	0.09
E_2	1.82 ± 0.05	0.11
E_3	2.72 ± 0.05	0.19

We now discuss the resonance Raman behavior of the 2LA band that comes from a second-order phonon process involving two phonons of the longitudinal acoustic (LA) branch near the Brillouin zone edge (K and M points) [43]. Figure 3b shows the REP of the 2LA mode, where the blue circles represent the experimental data and the curves represent the best fit considering the expression for the intensity of a second-order Raman process as a function of the laser energy E_L given by the following expression [43]:

$$I^{2LA}(E_L) = \sum_i \left| \frac{M_{\text{el-rad}} \cdot M_{\text{ex-ph}}^{(i)-LA} \cdot M_{\text{ex-ph}}^{(i)-LA} \cdot M_{\text{el-rad}}}{(E_L - E_{\text{ex}}^i - 2E_{\text{ph}}^{LA} - i\gamma^i)(E_L - E_{\text{ex}}^i - E_{\text{ph}}^{LA} - i\gamma^i)(E_L - E_{\text{ex}}^i - i\gamma^i)} \right|^2, \quad (2)$$

where the two middle terms in the numerator of Equation (2) represent the exciton–phonon interactions involving two phonons with opposite momenta. The denominator shows three terms that give the resonances of the incident photon and the scattered photon with one and two phonons. The REP of the 2LA Raman band shown in Figure 3b was fitted using the same energy values of E_1 , E_2 , and E_3 , shown in Table 1. We can observe that the 2LA band is significantly enhanced at lower energies (E_1 and E_2) but only very weakly enhanced at the higher energy resonance (E_3).

Figure 3c shows the photoluminescence spectra recorded at the dome center (upper spectrum), at the MoS₂ bulk substrate (middle spectrum), and the subtraction between the two first ones in the bottom, where we can only observe the contribution of the strained MoS₂ single layer.

4. Discussion

Let us now discuss the physical origin of the three resonances E_1 , E_2 , and E_3 observed in the resonance Raman results. For the first-order A'_1 and E' , we observed that the out-of-plane A'_1 mode is strongly enhanced at E_1 and E_3 , whereas the in-plane E' is only strongly enhanced at the higher resonance energy E_3 . On the other hand, the second-order 2LA band is significantly enhanced at E_1 and E_2 and practically not observed at E_3 .

The highest resonance energy E_3 can be attributed to exciton C of MoS₂, whose energy in unstrained monolayer MoS₂ is around 2.9 eV, as observed by resonance Raman spectroscopy [46], and is far isolated from the other lower energy excitons in the optical spectrum. The observed value of the C exciton energy at 2.72 eV allows us to conclude that it is redshifted by about 0.18 eV in the strained domes with respect to the unstrained MoS₂ monolayer, similar to the case of the energies of A and B excitons in the strained MoS₂ domes. Interestingly, the 2LA band is only very weakly enhanced at higher energies, thus revealing a weak interaction of the zone-edge LA phonons with the C exciton.

In order to assign the E_1 and E_2 resonances in the REPs, we acquired the photoluminescence (PL) spectrum on the same dome, whose REP curves are displayed in Figure 3a,b. The topmost trace in Figure 3c is the PL spectrum recorded with the laser spot centred on the top of the MoS₂ dome. The emission from the MoS₂ substrate (or bulk) adjacent to the dome is given by the middle trace in Figure 3c. Finally, the bottommost trace in Figure 3c is obtained by subtracting the bulk contribution from the spectrum recorded on the dome. It must be emphasized that the spectrum intensities were not corrected by the spectral response of the spectrometer (detector and gratings), and the intensities at lower energies are underestimated. Nevertheless, in the PL spectrum, two clear resonances are observed. They match the E_1 and E_2 REP resonances very well, which are indicated by the arrows in the lower part of Figure 3c.

Previous PL studies on strained MoS₂ domes similar to those investigated here showed the presence of two main contributions to the emission spectrum acquired close to the top of the dome [11], like in the present case. The lower and higher energy resonances in the PL spectrum were attributed to the indirect and direct excitons, respectively. As a matter of fact, for sufficiently high strain values (typically greater than 2%), the maximum of the valence band (VB) of the MoS₂ monolayer undergoes a transition from K to Γ (the same occurs in WS₂ and WSe₂ monolayers, as reported in ref. [11]). At the same time,

the minimum of the conduction band (CB) at K moves at lower energy, while remaining the lowest state of the CB. Consequently, the exciton transition with the lowest energy becomes indirect in character ($\Gamma_{VB} - K_{CB}$), while the direct exciton transition ($K_{VB} - K_{CB}$) is at higher energy. It should be noted though that when the direct and indirect excitons are resonant, they hybridize, and their direct vs indirect character is smeared out. In particular, the indirect exciton may gain sufficient oscillator strength and become bright despite its k-space indirect character. Recently, evidence of exciton hybridization was also observed in the strain dependence of the exciton magnetic moment in WS_2 domes [13]. By comparing the PL difference spectrum in Figure 3c with the results on MoS_2 domes reported in ref. [11], we may attribute the E_1 resonance in the REPs to the indirect exciton and the E_2 resonance to the direct exciton. Indeed, in ref. [11], it was observed that the indirect exciton energy ranges between 1.65 eV and 1.62 eV depending on the position on the dome, in agreement with the E_1 resonance. The direct exciton was found to vary from 1.75 eV to 1.78 eV for increasing strain, which suggests the E_2 resonance ($E_2 = 1.82 \pm 0.05$ eV) is associated with the direct (or A) exciton state. Nevertheless, due to the large energy uncertainty of E_2 and its low spectral weight, we cannot exclude a possible contribution from the B exciton. Notice that the energies of the A and B excitons obtained from the REPs of the Raman modes in the unstrained single layer of MoS_2 are 1.90 eV and 2.05 eV [46], showing that A and B exciton energies in MoS_2 domes are redshifted with respect to the case of unstrained 1L- MoS_2 .

Finally, the different relative weight of the indirect (corresponding to E_1) and direct (corresponding to E_2) excitons in the PL spectra and in the REP curves probably comes from the exciton–phonon interaction. The PL process involves two optical transitions, and the Raman process involves not only the two optical transitions but also the exciton–phonon interaction, whose matrix element is given by the middle term in the numerator of Equation (1), which is specific for each exciton i and phonon k .

5. Conclusions

In conclusion, this study presents a resonance Raman analysis of the first-order modes and of the double-resonance 2LA band in a dome of strained monolayer MoS_2 , using 23 different laser excitation energies in the range of 1.59 to 2.73 eV. It was observed that the Raman features are enhanced by three resonance energies, E_1 , E_2 , and E_3 at, respectively, 1.61 eV, 1.82 eV, and 2.72 eV. It was observed that the out-of-plane A'_1 mode is significantly enhanced by the first and the third resonances (E_1 and E_3), while the in-plane E' mode was only significantly enhanced at E_3 . The 2LA band, which comes from a double-resonance Raman process involving two phonons, exhibited a different resonance behavior, since it was strongly enhanced at the two first resonances E_1 and E_2 and practically not observed at E_3 . Our analysis allowed us to ascribe the third resonance to the C exciton of MoS_2 . On the other hand, the high strain values (about 5%) that can be reached in the MoS_2 domes led to a direct-to-indirect band gap transition, with the indirect exciton at lower energy than the direct (or A) exciton. As a matter of fact, the comparison between the strain-dependent PL spectra and the the REP curves indicated that the first and second resonances are consistent with the indirect and direct excitons, respectively. Our results show that the exciton–phonon coupling involving the out-of-plane A'_1 and the in-plane E' modes with the A exciton is small in strained MoS_2 . On the other hand, the enhancement of the first-order modes by the C exciton, especially strong for the E' mode, reveals a strong exciton–phonon coupling in this case. The second-order 2LA band exhibited a different resonance behavior, since it was significantly enhanced at the lower energy resonances but practically not observed when the excitation energy matched the exciton C, thus revealing the selective exciton–phonon interaction for the double-resonance Raman process of MoS_2 -type materials. These findings provide valuable insights into the behavior of MoS_2 under strain and its potential use in developing strain-based devices, and contribute to the existing knowledge of MoS_2 physical properties.

Author Contributions: Sample preparation, E.B. and A.P.; Raman and PL measurements, J.S.L.; project idealization and guidance, M.A.P., A.P. and A.R.; paper writing, J.S.L., M.A.P. and A.R. All authors have contributed to data analysis and writing of the paper. All authors have read and agreed to the final version of the manuscript.

Funding: We gratefully acknowledge the financial support provided by the following Brazilian institutions: Instituto Nacional de Ciência e Tecnologia (INCT) em Nanomateriais de Carbono, Financiadora de Estudos e Projetos (FINEP), Coordenação de Aperfeiçoamento de Pessoal de Nível Superior (CAPES), Conselho Nacional de Desenvolvimento Científico e Tecnológico (CNPq), and Fundação de Amparo à Pesquisa do Estado de Minas Gerais (FAPEMIG). Without their support, this work would not have been possible. This project was partly funded within the QuantERA II Programme that has received funding from the European Union's Horizon 2020 research and innovation programme under Grant Agreement No. 101017733, and with funding organisations Ministero dell'Università e della Ricerca (MUR) and Consiglio Nazionale delle Ricerche (CNR). We acknowledge financial support from the PNRR MUR project PE0000023-NQSTI.

Data Availability Statement: The data used to support the findings of this study can be made available by the corresponding author upon request.

Acknowledgments: We gratefully acknowledge the financial support provided by the following Brazilian institutions: Instituto Nacional de Ciência e Tecnologia (INCT) em Nanomateriais de Carbono, Financiadora de Estudos e Projetos (FINEP), Coordenação de Aperfeiçoamento de Pessoal de Nível Superior (CAPES), Conselho Nacional de Desenvolvimento Científico e Tecnológico (CNPq), and Fundação de Amparo à Pesquisa do Estado de Minas Gerais (FAPEMIG). Without their support, this work would not have been possible. This project was partly funded within the QuantERA II Programme that has received funding from the European Union's Horizon 2020 research and innovation programme under Grant Agreement No 101017733, and with funding organisations Ministero dell'Università e della Ricerca (MUR) and Consiglio Nazionale delle Ricerche (CNR). We acknowledge financial support from the PNRR MUR project PE0000023-NQSTI.

Conflicts of Interest: The authors declare no conflict of interest.

References

1. Hess, P. Bonding, structure, and mechanical stability of 2D materials: The predictive power of the periodic table. *Nanoscale Horiz.* **2021**, *6*, 856–892. [[CrossRef](#)]
2. Li, X.; Tao, L.; Chen, Z.; Fang, H.; Li, X.; Wang, X.; Xu, J.-B.; Zhu, H. Graphene and related two-dimensional materials: Structure-property relationships for electronics and optoelectronics. *Appl. Phys. Rev.* **2017**, *4*, 021306. [[CrossRef](#)]
3. Geim, A.; Grigorieva, I. Van der Waals heterostructures. *Nature* **2013**, *499*, 419–425. [[CrossRef](#)]
4. Butler, S.Z.; Hollen, S.M.; Cao, L.; Cui, Y.; Gupta, J.A.; Gutiérrez, H.R.; Heinz, T.F.; Hong, S.S.; Huang, J.; Ismach, A.F.; et al. Progress, Challenges, and Opportunities in Two-Dimensional Materials Beyond Graphene. *ACS Nano* **2013**, *7*, 2898–2926. [[CrossRef](#)]
5. Blundo, E.; Cappelluti, E.; Felici, M.; Pettinari, G.; Polimeni, A. Strain-tuning of the electronic, optical, and vibrational properties of two-dimensional crystals. *Appl. Phys. Rev.* **2021**, *8*, 021318. [[CrossRef](#)]
6. Yang, S.; Chen, Y.; Jiang, C. Strain engineering of two-dimensional materials: Methods, properties, and applications. *InfoMat* **2021**, *3*, 397–420. [[CrossRef](#)]
7. Dai, Z.; Liu, L.; Zhang, Z. Strain Engineering of 2D Materials: Issues and Opportunities at the Interface. *Adv. Mater.* **2019**, *31*, 1805417. [[CrossRef](#)] [[PubMed](#)]
8. Roldán, R.; Castellanos-Gomez, A.; Cappelluti, E.; Guinea, F. Strain engineering in semiconducting two-dimensional crystals. *J. Phys. Condens. Matter* **2015**, *27*, 313201. [[CrossRef](#)]
9. Di Giorgio, C.; Blundo, E.; Pettinari, G.; Felici, M.; Bobba, F.; Polimeni, A. Mechanical, Elastic, and Adhesive Properties of Two-Dimensional Materials: From Straining Techniques to State-of-the-Art Local Probe Measurements. *Adv. Mater. Interfaces* **2022**, *9*, 2102220. [[CrossRef](#)]
10. Guinea, F.; Katsnelson, M.; Geim, A. Energy gaps; a zero-field quantum Hall effect in graphene by strain engineering. *Nat. Phys.* **2010**, *6*, 30–33. [[CrossRef](#)]
11. Blundo, E.; Felici, M.; Yildirim, T.; Pettinari, G.; Tedeschi, D.; Miriametro, A.; Liu, B.; Ma, W.; Lu, Y.; Polimeni, A. Evidence of the direct-to-indirect band gap transition in strained two-dimensional WS₂, MoS₂ and WSe₂. *Phys. Rev. Res.* **2020**, *2*, 012024. [[CrossRef](#)]
12. Frisenda, R.; Drüppel, M.; Schmidt, R.; Michaelis de Vasconcellos, S.; Perez de Lara, D.; Bratschitsch, R.; Rohlfing, M.; Castellanos-Gomez, A. Biaxial strain tuning of the optical properties of single-layer transition metal dichalcogenides. *Npj 2D Mater. Appl.* **2017**, *1*, 10. [[CrossRef](#)]

13. Blundo, E.; Faria Junior, P.E.; Surrente, A.; Pettinari, G.; Prosnikov, M.A.; Olkowska-Pucko, K.; Zollner, K.; Woźniak, T.; Chaves, A.; Kazimierczuk, T.; et al. Strain-Induced Exciton Hybridization in WS₂ Monolayers Unveiled by Zeeman-Splitting Measurements. *Phys. Rev. Lett.* **2022**, *129*, 067402. [[CrossRef](#)] [[PubMed](#)]
14. Li, F.; Shen, T.; Xu, L.; Hu, C.; Qi, J. Strain Improving the Performance of a Flexible Monolayer MoS₂ Photodetector. *Adv. Electron. Mater.* **2019**, *5*, 1900803. [[CrossRef](#)]
15. Datye, I.M.; Daus, A.; Grady, R.W.; Brenner, K.; Vaziri, S.; Pop, E. Strain-Enhanced Mobility of Monolayer MoS₂. *Nano Lett.* **2022**, *22*, 8052–8059. [[CrossRef](#)]
16. He, K.; Poole, C.; Mak, K.F.; Shan, J. Experimental Demonstration of Continuous Electronic Structure Tuning via Strain in Atomically Thin MoS₂. *Nano Lett.* **2013**, *13*, 2931–2936. [[CrossRef](#)]
17. Scalise, E.; Houssa, M.; Pourtois, G.; Afanas'ev, V.; Stesmans, A. Strain-induced semiconductor to metal transition in the two-dimensional honeycomb structure of MoS₂. *Nano Res.* **2012**, *5*, 43–48. [[CrossRef](#)]
18. Johari, P.; Shenoy, V.B. Tuning the Electronic Properties of Semiconducting Transition Metal Dichalcogenides by Applying Mechanical Strains. *ACS Nano* **2012**, *6*, 5449–5456. [[CrossRef](#)] [[PubMed](#)]
19. Guzman, D.M.; Strachan, A. Role of strain on electronic and mechanical response of semiconducting transition-metal dichalcogenide monolayers: An ab-initio study. *J. Appl. Phys.* **2014**, *115*, 243701. [[CrossRef](#)]
20. Scalise, E.; Houssa, M.; Pourtois, G.; Afanas'ev, V.V.; Stesmans, A. First-principles study of strained 2D MoS₂. *Phys. E Low-Dimens. Syst. Nanostruct.* **2014**, *56*, 416–421. [[CrossRef](#)]
21. Nguyen, C.V.; Hieu, N.N. Effect of biaxial strain and external electric field on electronic properties of MoS₂ monolayer: A first-principle study. *Chem. Phys.* **2016**, *468*, 9–14. [[CrossRef](#)]
22. Zollner, K.; Junior, P.E.F.; Fabian, J. Strain-tunable orbital, spin-orbit, and optical properties of monolayer transition-metal dichalcogenides. *Phys. Rev. B* **2019**, *100*, 195126. [[CrossRef](#)]
23. Lee, C.; Wei, X.; Kysar, J.W.; Hone, J. Measurement of the Elastic Properties and Intrinsic Strength of Monolayer Graphene. *Science* **2008**, *321*, 385–388. [[CrossRef](#)]
24. Bertolazzi, S.; Brivio, J.; Kis, A. Stretching and Breaking of Ultrathin MoS₂. *ACS Nano* **2011**, *5*, 9703–9709. [[CrossRef](#)]
25. Deng, S.; Sumant, A.V.; Berry, V. Strain engineering in two-dimensional nanomaterials beyond graphene. *Nano Today* **2018**, *22*, 14–35. [[CrossRef](#)]
26. Guo, H.; Yang, T.; Tao, P.; Wang, Y.; Zhang, Z. High pressure effect on structure, electronic structure, and thermoelectric properties of MoS₂. *J. Appl. Phys.* **2013**, *113*, 013709. [[CrossRef](#)]
27. Tao, P.; Guo, H.; Yang, T.; Zhang, Z. Strain-induced magnetism in MoS₂ monolayer with defects. *J. Appl. Phys.* **2014**, *115*, 054305. [[CrossRef](#)]
28. Zhang, Y.; Guo, H.; Sun, W.; Sun, H.; Ali, S.; Zhang, Z.; Saito, R.; Yang, T. Scaling law for strain dependence of Raman spectra in transition-metal dichalcogenides. *J. Raman Spectrosc.* **2020**, *51*, 1–9. [[CrossRef](#)]
29. Zhao, Y.; Zhang, S.; Xu, B.; Zhang, S.; Han, S.; Zhang, J.; Tong, L. Monitoring Strain-Controlled Exciton-Phonon Coupling in Layered MoS₂ by Circularly Polarized Light. *J. Phys. Chem. Lett.* **2021**, *12*, 11555–11562. [[CrossRef](#)]
30. Xiao, D.; Liu, G.-B.; Feng, W.; Xu, X.; Yao, W. Coupled Spin and Valley Physics in Monolayers of MoS₂ and Other Group-VI Dichalcogenides. *Phys. Rev. Lett.* **2012**, *108*, 196802. [[CrossRef](#)] [[PubMed](#)]
31. Amorim, B.; Cortijo, A.; de Juan, F.; Grushin, A.G.; Guinea, F.; Gutiérrez-Rubio, A.; Ochoa, H.; Parente, V.; Roldán, R.; San-Jose, P.; et al. Novel effects of strains in graphene and other two dimensional materials. *Phys. Rep.* **2016**, *617*, 1–54. [[CrossRef](#)]
32. Lloyd, D.; Liu, X.; Christopher, J.W.; Cantley, L.; Wadehra, A.; Kim, B.L.; Goldberg, B.B.; Swan, A.K.; Bunch, J.S. Band Gap Engineering with Ultralarge Biaxial Strains in Suspended Monolayer MoS₂. *Nano Lett.* **2016**, *16*, 5836–5841; Correction in *Nano Lett.* **2019**, *19*, 7548–7548. [[CrossRef](#)] [[PubMed](#)]
33. Li, H.; Tsai, C.; Koh, A.L.; Cai, L.; Contryman, A.W.; Fragapane, A.H.; Zhao, J.; Han, H.S.; Manoharan, H.C.; Abild-Pedersen, F.; et al. Activating and optimizing MoS₂ basal planes for hydrogen evolution through the formation of strained sulphur vacancies. *Nat. Mater.* **2016**, *15*, 48–53. [[CrossRef](#)] [[PubMed](#)]
34. Chaste, J.; Missaoui, A.; Huang, S.; Henck, H.; Ben Aziza, Z.; Ferlazzo, L.; Naylor, C.; Balan, A.; Johnson, A.T.C., Jr.; Braive, R.; et al. Intrinsic Properties of Suspended MoS₂ on SiO₂/Si Pillar Arrays for Nanomechanics and Optics. *ACS Nano* **2018**, *12*, 3235–3242. [[CrossRef](#)]
35. Xie, S.; Tu, L.; Han, Y.; Huang, L.; Kang, K.; Lao, K.U.; Poddar, P.; Park, C.; Muller, D.A.; Distasio, R.A.; et al. Coherent, atomically thin transition-metal dichalcogenide superlattices with engineered strain. *Science* **2018**, *359*, 1131–1136. [[CrossRef](#)]
36. Blundo, E.; Di Giorgio, C.; Pettinari, G.; Yildirim, T.; Felici, M.; Lu, Y.; Bobba, F.; Polimeni, A. Engineered Creation of Periodic Giant, Nonuniform Strains in MoS₂ Monolayers. *Adv. Mater. Interfaces* **2020**, *7*, 2000621. [[CrossRef](#)]
37. Conley, H.J.; Wang, B.; Ziegler, J.I.; Haglund, R.F., Jr.; Pantelides, S.T.; Bolotin, K.I. Bandgap Engineering of Strained Monolayer and Bilayer MoS₂. *Nano Lett.* **2013**, *13*, 3626–3630. [[CrossRef](#)]
38. Tedeschi, D.; Blundo, E.; Felici, M.; Pettinari, G.; Liu, B.; Yildirim, T.; Petroni, E.; Zhang, C.; Zhu, Y.; Sennato, S.; et al. Controlled Micro/Nanodome Formation in Proton-Irradiated Bulk Transition-Metal Dichalcogenides. *Adv. Mater.* **2019**, *31*, 1903795. [[CrossRef](#)]
39. Pimenta, M.A.; del Corro, E.; Carvalho, B.R.; Fantini, C.; Malard, L.M. Comparative Study of Raman Spectroscopy in Graphene and MoS₂-type Transition Metal Dichalcogenides. *Accounts Chem. Res.* **2015**, *48*, 41–47. [[CrossRef](#)]
40. Zhang, X.; Qiao, X.-F.; Shi, W.; Wu, J.-B.; Jiang, D.-S.; Tan, P.-H. Phonon and Raman scattering of two-dimensional transition metal dichalcogenides from monolayer, multilayer to bulk material. *Chem. Soc. Rev.* **2015**, *44*, 2757–2785. [[CrossRef](#)]

41. Li, H.; Zhang, Q.; Yap, C.C.R.; Tay, B.K.; Edwin, T.H.T.; Olivier, A.; Baillargeat, D. From Bulk to Monolayer MoS₂: Evolution of Raman Scattering. *Adv. Funct. Mater.* **2012**, *22*, 1385–1390. [[CrossRef](#)]
42. R Saito, R.; Tatsumi, Y.; Huang, S.; Ling, X.; Dresselhaus, M.S. Raman spectroscopy of transition metal dichalcogenides. *J. Phys. Condens. Matter* **2016**, *28*, 353002. [[CrossRef](#)]
43. Carvalho, B.R.; Wang, Y.; Mignuzzi, S.; Roy, D.; Terrones, M.; Fantini, C.; Crespi, V.H.; Malard, L.M.; Pimenta, M.A. Intervalley scattering by acoustic phonons in two-dimensional MoS₂ revealed by double-resonance Raman spectroscopy. *Nat. Commun.* **2017**, *8*, 14670. [[CrossRef](#)] [[PubMed](#)]
44. Seguini, G.; Schamm-Chardon, S.; Pellegrino, P.; Perego, M. The energy band alignment of Si nanocrystals in SiO₂. *Appl. Phys. Lett.* **2011**, *99*, 082107. [[CrossRef](#)]
45. Garvie, L.A.J.; Pez, P.; Alvarez, J.R.; Buseck, P.R.; Craven, A.J.; Brydson, R. Bonding in alpha-quartz (SiO₂): A view of unoccupied states. *Am. Mineral.* **2000**, *85*, 732–738. [[CrossRef](#)]
46. Carvalho, B.R.; Malard, L.M.; Alves, J.M.; Fantini, C.; Pimenta, M.A. Symmetry-Dependent Exciton-Phonon Coupling in 2D and Bulk MoS₂ Observed by Resonance Raman Scattering. *Phys. Rev. Lett.* **2015**, *114*, 136403; Erratum in *Phys. Rev. Lett.* **2016**, *116*, 089904. [[CrossRef](#)]

Disclaimer/Publisher's Note: The statements, opinions and data contained in all publications are solely those of the individual author(s) and contributor(s) and not of MDPI and/or the editor(s). MDPI and/or the editor(s) disclaim responsibility for any injury to people or property resulting from any ideas, methods, instructions or products referred to in the content.